

A *CHANDRA* PROPER MOTION FOR PSR J1809–2332

ADAM VAN ET TEN¹, ROGER W. ROMANI¹, AND C.-Y. NG^{2,3}

¹ Department of Physics, Stanford University, Stanford, CA 94305, USA; rwr@astro.stanford.edu

² Department of Physics, McGill University, Montreal, QC H3A 2T8, Canada
 Received 2012 May 18; accepted 2012 July 2; published 2012 August 6

ABSTRACT

We report on a new *Chandra* exposure of PSR J1809–2332, the recently discovered pulsar powering the bright EGRET source 3EG J1809–2328. By registration of field X-ray sources in an archival exposure, we measure a significant proper motion for the pulsar point source over an ≈ 11 yr baseline. The shift of 0.30 ± 0.06 (at P.A. = 153.3 ± 18.4) supports an association with proposed supernova remnant (SNR) parent G7.5–1.7. Spectral analysis of diffuse emission in the region also supports the interpretation as a hard wind nebula trail pointing back toward the SNR.

Key words: pulsars: individual (PSR J1809-2332) – X-rays: general

Online-only material: color figures

1. INTRODUCTION

3EG J1809–2328 was one of the brightest unidentified hard-spectrum gamma-ray sources detected by EGRET (Hartman et al. 1999). *ASCA* observations of the EGRET error box revealed an extended X-ray source (Roberts et al. 2001), suggestive of a pulsar wind nebula (PWN). A 9.7 ks *Chandra* ACIS exposure in 2000 August (Braje et al. 2002) revealed a point source connected to the non-thermal X-ray/radio nebula, bolstering the PWN identification. Roberts & Brogan (2008) then described G7.5–1.7, a partial ~ 0.5 – 0.8 radius radio shell and possible supernova remnant (SNR); the center of this SNR candidate lies 0.3 from the point source, in the general direction defined by the PWN trail.

The PSR/PWN nature of the source was confirmed by the discovery of PSR J1809–2332, a $P = 147$ ms, $\tau_c = 68$ kyr pulsar discovered by blind search of the *Fermi* Large Area Telescope (LAT) γ -ray photons (Abdo et al. 2009). This energetic ($\dot{E} = 4.3 \times 10^{35}$ erg s^{−1}) pulsar powers the γ -ray and PWN emission and has a timing position consistent with the X-ray point source at the PWN apex (Ray et al. 2011). As for most γ -ray-selected pulsars, we lack a dispersion measure estimate of the distance. However, Oka et al. (1999) suggested that the diffuse X-ray emission is anti-correlated with molecular gas in the Lynds 227 dark cloud; if associated this implies a plausible $d \sim 1.8$ kpc.

To test the SNR association and to improve spectral and morphological measurements of the diffuse emission, we have obtained a new *Chandra* ACIS exposure. By carefully matching to the original pointing, we have minimized systematic effects and allowed excellent frame referencing and astrometry of the point source. The ~ 11 yr baseline between the exposures thus allows a sensitive study of the proper motion and origin of PSR J1809–2332.

2. X-RAY DATA ANALYSIS

PSR J1809–2332 was observed on 2011 July 28 (ObsID 12546) for 29.7 ks in timed VFaint mode. As for our 2000 August 16 exposure (ObsID 739) we used the ACIS-I array. To

minimize changes in the reference star point spread functions (PSFs) (see below) we matched the roll angle to the 2000 epoch. The point-source position was not, of course, known in the initial exposure and fell rather close to a chip boundary. We thus shifted the pointing $\sim 30''$ in each coordinate to move the point source further onto the I3 chip and improve measurement of diffuse emission in its vicinity. The data were analyzed with CIAO 4.3, after re-processing both frames to the most current ACIS calibration. No flaring occurred during ObsID 12546, so the full 29.7 ks was used. For ObsID 739, the full 9.7 ks was also usable.

After combining, exposure correcting (with *fluximage*), and adaptive smoothing, the ACIS-I frame gives a good overall view of the pulsar vicinity (Figure 1). There is appreciable diffuse X-ray emission across the center of the image. The pulsar point source lies near the apex of a patch of brighter nebulosity that trails off to the northwest for $\sim 5'$. On smaller scales the PWN has a bright core behind the pulsar, $\sim 3''$ – $5''$ extension transverse to this trail at the point source and fainter diffuse emission “ahead” of the pulsar. To the south of the pulsar, numerous bright X-ray sources from the young star cluster S32 are seen. These bright stars provide excellent sources to aid frame registration between epochs. There are some low-significance X-ray concentrations outside of the bright inner nebula in Figure 1(b). None have obvious stellar counterparts so it is unclear if these are background sources or clumps in the diffuse nebular emission.

3. FRAME POINTING OFFSET

To best constrain any pulsar proper motion, we must optimally register the two observation epochs, using field point sources. We identify these using the CIAO *wavdetect* tool, selecting sources with a significance ≥ 5 in both observations. The young S32 star cluster $\sim 8'$ due south of the pulsar provides the bulk of the reference stars; inevitably several bright stars fall into chip gaps in one or the other of the observations, precluding their use. This leaves 14 stellar sources, plus the pulsar. We label the reference stars by increasing physical pixel x -coordinate (decreasing R.A.), mark these in Figure 1(a) and tabulate the *wavdetect* pixel positions and significances for each epoch in Table 1.

³ Tomlinson Postdoctoral Fellow, CRAQ Postdoctoral Fellow.

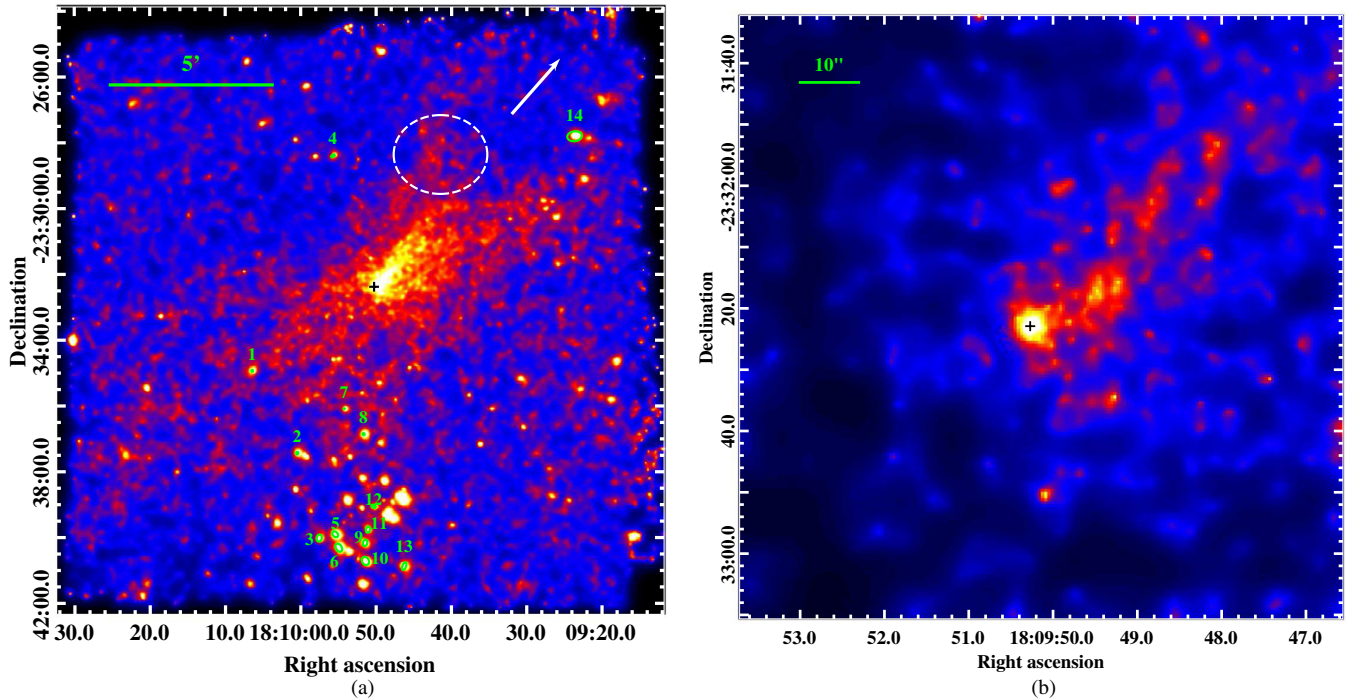


Figure 1. Left: merged *Chandra* exposure-corrected 0.5–7 keV ACIS-I array image of the extended emission around PSR J1809–2332 (observation IDs 739, 12546), adaptively smoothed (0.5–15 pixel Gaussian kernels, 10^{-6} erg cm $^{-2}$ s $^{-1}$ flux minimum). A possible bow shock and trail are seen extending northwest from the pulsar. Point sources used in frame matching are shown in green, with the pulsar position marked with a black plus symbol. The white ellipse denotes the 1σ error ellipse for the extrapolated pulsar position some 10 kyr in the past, while the white arrow points to the proposed explosion site for SNR G7.5–1.7. These two directions agree within 1σ . Right: merged adaptively smoothed (0.5–15 pixel Gaussian kernels, 3 count minimum) 0.5–7 keV image of the 100'' surrounding the pulsar. Both panels are displayed with a logarithmic stretch.

(A color version of this figure is available in the online journal.)

Table 1
Wavdetect Source Positions

Source	Obs1 X	Obs1 Y	Obs1 Sig	Obs2 X	Obs2 Y	Obs2 Sig
1	3727.7 \pm 0.2	3830.9 \pm 0.3	8.9	3796.6 \pm 0.1	3892.5 \pm 0.1	34.3
2	3894.4 \pm 0.2	3527.3 \pm 0.3	35.4	3963.4 \pm 0.3	3587.3 \pm 0.4	6.0
3	3971.2 \pm 0.7	3213.6 \pm 0.8	5.9	4044.7 \pm 0.5	3272.7 \pm 0.6	11.6
4	4026.8 \pm 0.4	4628.9 \pm 0.5	5.4	4095.9 \pm 0.4	4689.4 \pm 0.3	11.9
5	4035.3 \pm 0.4	3225.6 \pm 0.4	24.4	4104.2 \pm 0.2	3286.5 \pm 0.2	42.4
6	4049.1 \pm 0.5	3177.4 \pm 0.4	24.1	4116.4 \pm 0.4	3238.1 \pm 0.5	15.7
7	4068.0 \pm 0.2	3691.5 \pm 0.3	6.1	4137.6 \pm 0.2	3752.1 \pm 0.2	11.8
8	4140.3 \pm 0.2	3597.1 \pm 0.2	31.7	4209.4 \pm 0.1	3657.8 \pm 0.1	51.0
9	4144.9 \pm 0.9	3194.2 \pm 0.9	6.0	4215.1 \pm 0.5	3254.8 \pm 0.8	6.0
10	4149.2 \pm 0.5	3125.5 \pm 0.5	17.8	4216.1 \pm 0.7	3187.9 \pm 0.8	8.2
11	4153.8 \pm 1.0	3244.0 \pm 0.9	5.7	4225.9 \pm 0.6	3303.8 \pm 0.8	6.1
12	4176.4 \pm 1.1	3327.8 \pm 1.0	5.2	4246.8 \pm 0.6	3389.5 \pm 0.4	8.5
13	4289.4 \pm 1.2	3108.4 \pm 1.0	7.3	4360.0 \pm 0.5	3168.4 \pm 0.9	5.2
14	4922.8 \pm 0.9	4702.8 \pm 1.1	7.6	4991.8 \pm 0.7	4762.0 \pm 0.5	17.7
PSR	4179.65 \pm 0.12	4143.61 \pm 0.13	29.5	4248.44 \pm 0.06	4204.07 \pm 0.06	59.1

The wavdetect tool uses “Mexican hat” wavelet functions of different scales to generate a source list and estimate position. This approximation may be inadequate far from the ACIS aimpoint where the mirror PSF induces substantial and systematic changes in the point-source count distribution. By approximately matching the pointing and roll angle we have kept the change in such distortions minimal between the two frames. Nevertheless, the PSF shape changes across the frame are very large and the majority of our reference stars lie $\geq 6'$ from the aimpoint and pulsar. We have improved the astrometric accuracy and further reduced the effect of the PSF variation by creating a simulated PSF for each point source and using these to fit the source position.

We extract the spectrum of each source with the specextract function, fitting the stellar point sources to an absorbed Mekal plasma model, and save this spectrum within the Sherpa plotting program with the save-chart-spectrum command. After re-scaling by $100\times$ to improve PSF modeling statistics, the spectra are passed to CHaRT⁴, which is a web interface to the SAOSac raytrace code. CHaRT also takes as input the exposure time as well as the source position, which is assumed to be the wavdetect position. The output of CHaRT is subsequently input into MARX to create model PSF events files at each source

⁴ <http://cxc.harvard.edu/chart/runchart.html>

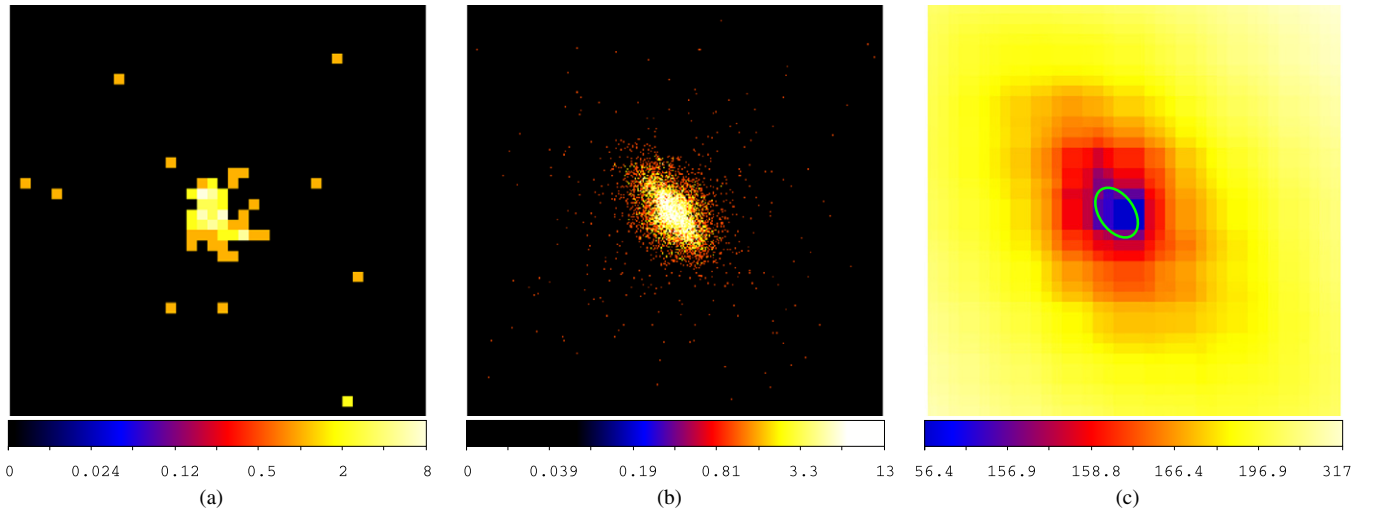


Figure 2. (a) *Chandra* events cutout of Source 8 (2011 epoch). (b) Simulated PSF at this source position. (c) Computed FoM map zoomed 10 \times , the green $\delta\text{FoM} = 0.5$ contour is shown. The extrema in x and y of this ellipse give the positional uncertainty in the source position. (A color version of this figure is available in the online journal.)

position, corrected for the offset of the science instrument module (SIM) from the nominal location.

The modeled source events are binned to 1/8 of the native ACIS pixel resolution and recorded in 320×320 image files. These are compared with data cutouts with matched 40×40 native-pixel images. PSF models and data cutouts are prepared for each star in both frames. We use these to solve for PSF versus data position shifts. The fitting program uses a maximum likelihood “figure of merit” (FoM, the negative \ln Poisson probability of getting the observed data counts from the model PSF), where we run a grid of trial positions shifted at the 1/8-pixel PSF model resolutions and sum the model counts to the observed ACIS pixel. The result is a map of source likelihood in PSF position shift x and y (relative to the nominal wavdetect location). An example of the cutout, PSF model, and shift map are shown in Figure 2.

In order to compute the best-fit position of the source, we fit an elliptic paraboloid to the FoM surface. The minimum of this surface determines the best-fit offset, and the offset error is estimated from the δFoM contours. As with Source 8, several of the ellipses had large axis ratios. However, an attempt to improve registration by fitting along the major and minor axes did not reduce the scatter. Thus to be conservative, we project the ellipses to the x and y pixel axes and fit in this unrotated space. We determine that 1σ (wavdetect) errors correspond to a $\delta\text{FoM} = 0.5$, and thus ascribe 1σ error ellipses to the region enclosed by this FoM increase above the fit minimum. Comparison with sources near the aimpoint, where a circular Mexican hat should be an adequate approximation, confirms that this provides a good error estimate. A typical fit and uncertainty are shown by the green ellipse in Figure 2.

Table 2 gives the PSF-fit-computed pixel offset of each source from the wavdetect position, along with estimates for the position errors. The mean offset of all reference sources (≈ 0.05 pixels) is not significantly different from zero in either axis, showing that the wavdetect solutions do not impose any large systematic offset between our matched exposures.

We can now use our stellar position estimates to register the frames. For the wavdetect positions we use the values in Table 1 directly. For PSF fits we add the additional offsets of Table 2 and use PSF localization errors. For each source i , we define,

Table 2
PSF Fit Offsets from Wavdetect Positions

Source	Obs1 (X, Y)	Obs2 (X, Y)
1	$(-0.17 \pm 0.26, +0.53 \pm 0.38)$	$(+0.08 \pm 0.12, -0.18 \pm 0.15)$
2	$(-0.01 \pm 0.18, -0.16 \pm 0.24)$	$(-0.22 \pm 0.52, +0.28 \pm 0.67)$
3	$(+1.61 \pm 1.68, -1.59 \pm 1.46)$	$(-0.09 \pm 0.44, -2.05 \pm 0.85)$
4	$(+0.22 \pm 0.70, +0.19 \pm 0.62)$	$(+0.30 \pm 0.46, +0.35 \pm 0.37)$
5	$(+0.03 \pm 0.24, -0.26 \pm 0.33)$	$(+0.38 \pm 0.18, -0.09 \pm 0.22)$
6	$(-0.61 \pm 0.37, -0.24 \pm 0.39)$	$(+0.62 \pm 0.51, -0.24 \pm 0.49)$
7	$(+0.50 \pm 0.35, -0.77 \pm 0.44)$	$(-0.34 \pm 0.28, -0.13 \pm 0.32)$
8	$(-0.09 \pm 0.20, -0.06 \pm 0.23)$	$(+0.05 \pm 0.13, +0.11 \pm 0.14)$
9	$(+1.36 \pm 0.24, +0.07 \pm 0.36)$	$(-0.39 \pm 0.29, +0.17 \pm 0.33)$
10	$(-0.55 \pm 0.36, +0.10 \pm 0.46)$	$(+1.83 \pm 0.85, -1.46 \pm 0.83)$
11	$(+0.65 \pm 0.33, -0.51 \pm 0.54)$	$(-0.96 \pm 0.32, +1.01 \pm 0.28)$
12	$(-0.38 \pm 0.73, +0.68 \pm 0.82)$	$(-0.96 \pm 0.54, -0.46 \pm 0.45)$
13	$(-1.20 \pm 0.92, +1.40 \pm 0.96)$	$(-0.98 \pm 0.64, +1.24 \pm 0.60)$
14	$(+1.16 \pm 0.37, -1.05 \pm 0.39)$	$(+0.98 \pm 0.27, +0.02 \pm 0.21)$
PSR	$(-0.16 \pm 0.12, -0.11 \pm 0.12)$	$(+0.04 \pm 0.06, -0.15 \pm 0.06)$

e.g., x_i as the difference in x coordinate between old and new exposures; epoch positional errors are added in quadrature to give δx_i . The best-fit frame shift is determined by minimizing the $\chi^2 = \sum_{i=1}^{14} [(x_i - S_x)/\delta x_i]^2$ between frames, where S_x is the frame shift. Similar values are computed for the y coordinate.

Inspection of the tables shows that Source 3 has both a large shift between frames and a large PSF-fit error. We suspect that it may be a confused double with variable components (hence the poor PSF fit and large apparent shift). We thus omit this star from the registration, leaving 13 field stars. We also attempted recursive pruning of field stars with the largest remaining $\delta x_i/\sigma_{x_i}$ or $\delta y_i/\sigma_{y_i}$; as expected the nominal-fit errors decreased slightly (especially for the PSF-fit solution). However, the shifts were small and decreasing the number of fit stars may increase sensitivity to systematics. We thus conservatively retain all stars except the obvious outlier Source 3 and report the best-fit shifts and shift errors in Table 3. Although many of our reference stars are from the S32 cluster, comparison with the non-cluster stars does not show any large systematic shifts. This is as expected since typical $\sim 10 \text{ km s}^{-1}$ association velocities are small compared to the expected pulsar space velocity, as is

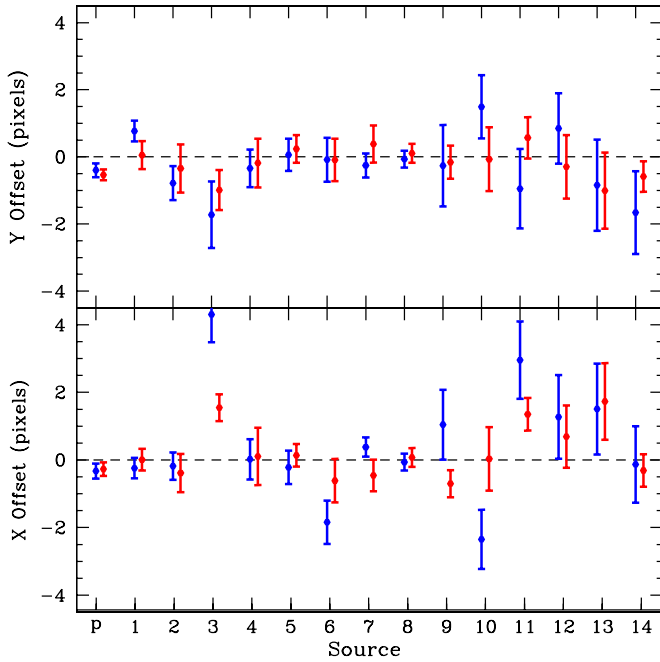


Figure 3. Residual source displacements between epochs (δ = new position – old position), relative to the PSF-fit frame offset (Table 3). Blue indicates wavdetect positions and errors, while red indicates positions and errors obtained from the FoM maps. Source 3, an obvious outlier, is pruned from the frame-shift fits. The pulsar shows small but significant shifts.

(A color version of this figure is available in the online journal.)

the velocity due to differential Galactic rotation, for the expected distances.

Table 3 lists the best-fit frame shifts for both the raw wavdetect positions and the PSF-fit positions. In both cases, we compute shifts only, adopting the *Chandra*-determined roll angle. The net pixel shifts are consistent between the two methods. However, the χ^2 and frame offset errors are significantly smaller for the PSF-fit approach. Figure 3 shows why the scatter of the PSF-fit position offsets about the best-fit line is smaller, with the exception of the obvious outlier Source 3. We thus adopt the PSF-fit measurements and offset. These finally allow us to compute the position shift (relative to the PSF-fit registration) of the pulsar between the two frames. The values for both wavdetect and improved PSF-fit detect centroiding are shown in Table 4. This table also gives the best-fit radial (in native ACIS

Table 3
Frame Offsets: Two Fit Methods

Method	Coordinates	Shift (pixel)	χ^2/dof
Wavdetect	X	69.12 ± 0.18	29.9/12
Wavdetect	Y	60.86 ± 0.15	16.2/12
PSF fit	X	69.17 ± 0.14	18.4/12
PSF fit	Y	60.83 ± 0.09	5.0/12

Table 4
Pulsar Displacement (2011.66–2000.71)

Method	X^a	Y^a	R^a (radial)	θ^b
Wavdetect	-0.33 ± 0.23	-0.40 ± 0.21	0.52 ± 0.15	140.6 ± 24.2
PSF fit	-0.27 ± 0.19	-0.54 ± 0.16	0.60 ± 0.13	153.3 ± 18.4

Notes.

^a pixels (1 pixel = $0''.49$).

^b Measured in degrees CCW from north.

pixel units) and P.A. shifts with propagated errors. In Figure 4 we show the registered frames near the pulsar, after shifting the 2000 epoch by (69.17, 60.83) pixels and regridding with the CIAO dmregrid2 function. The circle marks the best-fit 2000 position while the ellipse marks the 2011 epoch localization, including frame shift uncertainties. Between epochs the pulsar shows a significant 4.6σ shift. We thus have detected the proper motion of PSR J1809–2332; we comment on the implications below.

To determine the absolute position at the 2011 epoch, we computed a least-squares fit using the PSF-fit positions and the optical positions of their USNO B-1 counterparts to obtain a 2011.66 pulsar location of R.A.(2000.0) = 18:09:50.25 \pm 0.03, decl.(2000.0) = $-23:32:22.68 \pm 0.10$.

4. X-RAY SPECTRA

For our spectral study we define extraction regions for the several compact and extended sources. On the smallest scales these are a $2''$ point-source aperture and a $3''.5 \times 5''$ “Torus” ellipse, transverse to the major nebula axis. This small aperture is visible, but unlabeled in Figure 5. In this figure we label the larger scale spectral extraction apertures: a brightest nebula “Trail,” a surrounding “Inner Nebula,” and three large regions of low surface brightness (an “Upstream” region ahead of the

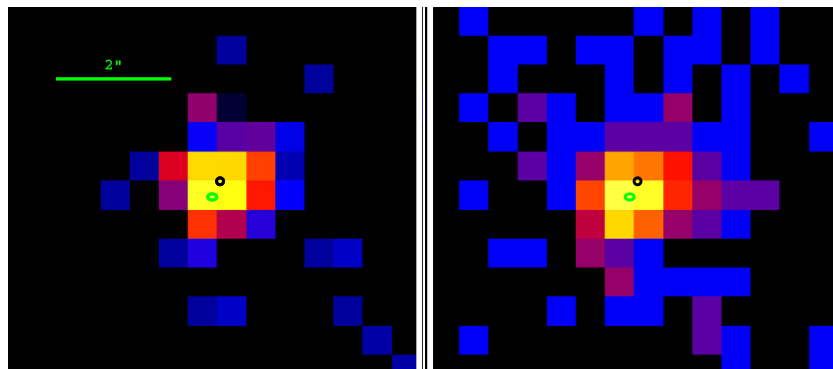
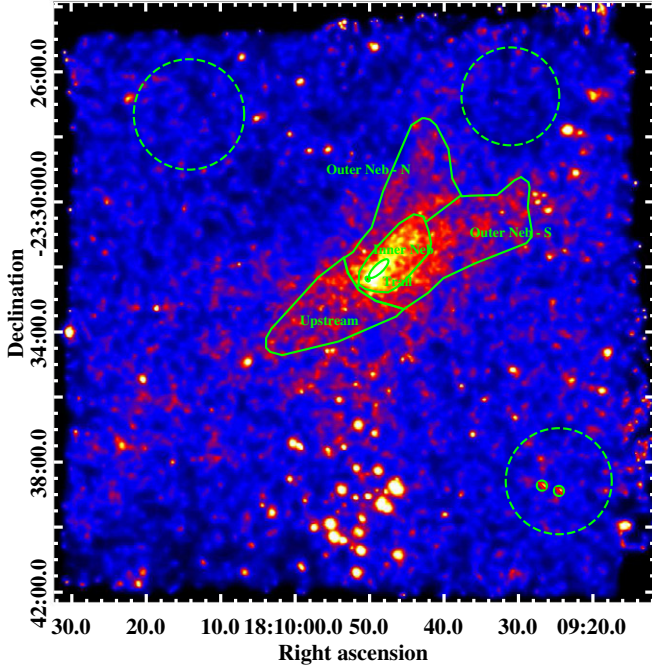


Figure 4. Left: *Chandra* image of the pulsar from the 2000 observation, registered to the 2011 frame. Right: matched *Chandra* image from the 2011 observation. Positions and errors (black circle: 2000; green ellipse: 2011) are taken from the FoM maps. The 2011 uncertainty includes the frame-tie errors added in quadrature (Table 3). The offset is significant at $\approx 4\sigma$.

(A color version of this figure is available in the online journal.)

Table 5
X-Ray Spectral Fits

Region	N_H^a	$\Gamma/\log T_{\text{eff}}$	Abs. Flux ^b	Unabs. Flux ^b	χ^2/dof
Trail+Inner	$1.31^{+0.20}_{-0.18}$	1.83 ± 0.16	$6.3^{+1.6}_{-1.2}$	$11.9^{+3.1}_{-2.3}$	112.9/199
PSR	1.3^c	$2.00 \pm 0.54/5.9 \pm 0.1$	$0.8^{+0.8}_{-0.4}$	$1.2^{+1.1}_{-0.6}$	12.7/26
Torus	1.3^c	$1.77^{+0.41}_{-0.38}$	$0.3^{+0.2}_{-0.1}$	$0.6^{+0.3}_{-0.2}$	5.3/8
Trail	1.3^c	$1.88^{+0.19}_{-0.18}$	0.9 ± 0.2	$1.8^{+0.4}_{-0.3}$	14.9/29
Inner Neb	1.3^c	1.79 ± 0.09	$4.6^{+0.5}_{-0.4}$	$8.4^{+0.9}_{-0.8}$	76.3/159
Upstream	1.3^c	$2.21^{+0.19}_{-0.18}$	2.3 ± 0.4	$5.4^{+1.0}_{-0.9}$	93.0/152
Upstream	$1.8^{+0.5}_{-0.4}$	$2.65^{+0.47}_{-0.41}$	$2.2^{+1.8}_{-0.9}$	$12.9^{+10.4}_{-5.4}$	91.6/151
Outer Neb	1.3^c	1.56 ± 0.10	$8.4^{+1.0}_{-0.9}$	$13.7^{+1.6}_{-1.5}$	196.6/348
Outer Neb-S	1.3^c	2.19 ± 0.14	3.9 ± 0.5	$9.0^{+1.2}_{-1.1}$	108.2/209
Outer Neb-S	1.8^c	2.61 ± 0.16	$3.7^{+0.6}_{-0.5}$	$13.3^{+2.0}_{-1.8}$	113.0/209
Outer Neb-N	1.3^c	1.00 ± 0.17	$4.3^{+1.0}_{-0.9}$	$5.8^{+1.3}_{-1.2}$	93.5/178

Notes.^a Interstellar absorption $\times 10^{22} \text{ cm}^{-2}$.^b 0.5–7 keV fluxes in units of $10^{-13} \text{ erg cm}^{-2} \text{ s}^{-1}$.^c Held fixed.**Figure 5.** Merged 0.5–7 keV image showing the spectral extraction regions and background regions (dotted). The torus region is too small to be clearly seen, but is a $3''.5 \times 5''$ ellipse centered on the pulsar and excising the inner $2''$.

(A color version of this figure is available in the online journal.)

pulsar and northern and southern extensions of the outer nebula). In each case the apertures exclude any enclosed smaller scale region. As noted in Section 3, we also extracted point-source spectra and fit absorbed Mekal models to the obvious stellar sources to derive spectra for computing model PSFs. These stellar sources were not exceptional and will not be discussed further here. Background regions are defined on source-free portions of the I0, I1, and I3 chips; scaled backgrounds are subtracted from the source spectra.

Spectra are extracted with the CIAO version 4.3 `specextract` function, which also computes response files. We group the spectra to a signal-to-noise ratio (S/N)/bin of 3, and fit all diffuse

regions jointly with old- and new-epoch data to an absorbed power-law model, using *Sherpa*. For the point source (pulsar) there is no evidence for variability, with $7.4 \pm 0.9 \times 10^{-3}$ cps during the first epoch and $7.6 \pm 0.5 \times 10^{-3}$ cps in the second. We therefore fit jointly to an absorbed power law plus a thermal component. Table 5 gives the fit values and 68% confidence errors. If we assume a common origin for the various components we can improve the spectral constraints by fitting for a global N_H . Using the brightest diffuse regions (Trail + Inner Nebula) we obtain $N_H = 1.3 \pm 0.2 \times 10^{22} \text{ cm}^{-2}$ and fix this for the other spectral regions. The Galactic HI surveys (nhtool) show a column of $\sim 5 \times 10^{21} \text{ cm}^{-2}$ to $d \sim 0.5$ kpc suggesting a source distance ≥ 1 kpc.

For the point source (neutron star), we first attempted a joint BB+PL fit, but found that the PL index was driven to very soft values $\Gamma > 6$, indicating a poor fit to the thermal spectrum. If fixed at a more physical $\Gamma = 2$ the fit is unacceptable. However, if we adopt a neutron star atmosphere model (*Sherpa* model `xsnsa`) we obtain a reasonable reduced χ^2 and power-law index. This model includes a number of parameters, three of which we fix: neutron star gravitation mass = $1.5 M_\odot$, neutron star radius = 10 km, and neutron star magnetic field = 10^{13} G. The remaining variables are the effective temperature and model normalization. The model normalization provides an estimate of the pulsar distance, which for the fitted parameters yields $d = 0.3^{+1.0}_{-0.1}$ kpc. This distance estimate is not very meaningful since, as usual, the thermal emission likely has contributions from a heated polar cap or soft magnetospheric power law. With the addition of such components the inferred distance increases; it is in any event consistent with the N_H constraint and the Oka et al. (1999) distance estimate.

The diffuse spectral indices are not atypical of hard PWN emission. We do not see any clear systematic softening as one moves farther from the pulsar. However, both the “Upstream” region and the “Outer Neb-S” appear significantly softer than the rest of the nebula. This is especially true if N_H is allowed to vary, when somewhat larger Γ values are preferred. The upstream emission is difficult to explain given the detected proper motion of the pulsar, unless it represents a foreground or background structure. This leads to the tentative suggestion that the hard-spectrum PWN is superposed on a softer background

arc composed of the “Upstream” and “Outer Neb-S” regions. This emission may be unrelated to the PWN. A plausible origin is a reverse shock structure in the SNR. Unfortunately, we lack adequate S/N to confirm the spectral differences or even to test whether a thermal fit is more suitable than a power-law model. In contrast, the “Outer Neb-N” region is formally very hard, quite distinct to the southern branch. Again the limited counts preclude any detailed spectral study.

5. DISCUSSION AND CONCLUSIONS

The displacement of 0.60 ± 0.13 pixels over 10.95 yr gives a proper motion of $\mu = 27 \pm 5$ mas yr⁻¹. This corresponds to a space velocity of $231 \pm 46(d/1.8 \text{ kpc}) \text{ km s}^{-1}$, a modest young pulsar space velocity. Interestingly, the proper motion vector points back to the birthsite of $l = 7^\circ 53$, $b = -1^\circ 68$ inferred within the $\sim 1^\circ 5$ diameter radio shell G7.5–1.7 by Roberts & Brogan (2008). This is $1300''$ from the pulsar so, taken at face value, our proper motion implies a kinematic age of 48 ± 10 kyr. Given the characteristic age $\tau_c = 68$ kyr, one gets an initial spin period $P_0 \sim 104 \pm 20$ ms for a braking index $n = 3$.

As noted by Roberts & Brogan (2008), the pulsar-projected offset is only $\sim 45\%$ of the SNR radius, so if the PWN lies in the SNR interior it may be just passing from being “crushed” by the reverse shock to forming a well-defined bow shock (van der Swaluw, Downes & Keegan 2004). Accordingly, we should not be too surprised that the morphology at the PWN apex (Figure 1(b)) is unclear. Certainly the bulk of the hard spectrum emission trails the pulsar, following the proper motion axis and the direction to the explosion site. However, there are significant counts bracketing the point source and extending $\sim 5''$ transverse to the pulsar motion. Since the pulsar spin axis appears to correlate with the proper motion (Johnston et al. 2005; Ng & Romani 2007) such transverse extension tends to be equatorial. It is tempting to infer that the blocky PWN head is the result of an anisotropic pulsar wind, concentrated in an equatorial torus, with a spin axis/Earth line-of-sight angle $\zeta \geq 75^\circ$, i.e., a torus viewed at large inclination angle. It is interesting to compare with predictions for the observed γ -ray pulse, which is a fairly narrow double with peak separation $\Delta = 0.35$. Examining the “Atlas” of Romani & Watters (2010), we see that γ -ray pulsars with $\Delta \approx 0.35$ should have $70^\circ > \zeta > 80^\circ$ and magnetic axis inclination $\alpha < 60^\circ$ for outer-magnetosphere-dominated emission. There is little phase space for such pulsars to be radio detected. Two-pole caustic (TPC)-type models produce such Δ for a wide range of $\zeta < 70^\circ$, but many of the solutions should be radio detected. Thus both model classes are allowed, although an outer-gap-type interpretation seems preferred. A good measurement of ζ from a detailed map of the PWN head could check this interpretation, but would require a rather long ACIS exposure.

Looking ahead of this transverse structure, we see that the hard-spectrum diffuse emission has a fairly abrupt cutoff at $\sim 1''$ (Figure 1(b)). We can compare this with the standoff angle for an isotropic ram-pressure-confined pulsar wind,

$$\theta_{\text{BS}} \approx \left(\frac{\dot{E}}{4\pi c \rho v^2 d^2} \right)^{1/2} \approx 1''.3 n^{-1/2} d_{1.8}^{-2}, \quad (1)$$

for our measured proper motion, an ambient number density $n \text{ cm}^{-3}$, and a distance 1.8 kpc. It seems that a small standoff is not unexpected, but given the apparent anisotropy in the wind momentum and likely anisotropy in the SNR interior, no strong conclusions should be drawn.

Of course there is emission “Upstream,” ahead of the pulsar motion. The chip gap spanned this region in the 2000 data so it was difficult to draw morphological conclusions. In the combined data it seems that this emission is morphologically distinct to, and substantially softer than, the PWN trail. This larger-scale soft emission is also seen in archival *XMM* and *ASCA* data where it also appears distinct from the harder PWN trail. In our data it appears to connect to the “Outer Neb-S” region, so we can posit that this extended softer emission may be a background or foreground structure associated with the host SNR. If the absorption is left free, these regions seem to prefer a slightly higher N_{H} than the central PWN. Given the extensive patchy molecular gas and obscuration in this region, these small differences are not particularly telling.

We have examined a new *Chandra* ACIS exposure of PSR J1809–2332 to study the fine scale X-ray morphology. Comparison with the 2000 exposure yields a $>4\sigma$ detection of the pulsar proper motion and supports the association with SNR G7.5–1.7. The PWN has slightly extended emission at the apex, somewhat larger than expected from a bow shock. While this suggests that the pulsar wind is concentrated transverse to its velocity, the possibility of anisotropies in the SNR interior discourages strong conclusions and such disturbed morphology is not unexpected. Overall, however, these new data support a basic picture for the PSR J1809–2332 system: a ~ 50 kyr pulsar viewed near the spin equator, but with small magnetic inclination so that the radio beam misses the Earth. The pulsar, traveling at $\sim 230 \text{ km s}^{-1}$, is followed by a trail of hard PWN X-ray emission and is approaching the outer region of its composite host SNR located at $d \leq 2$ kpc.

This work was supported in part by *Chandra* grant G01-12073X issued by the Chandra X-Ray Center, which is operated by the Smithsonian Astrophysical Observatory for and on behalf of the National Aeronautics Space Administration under contract NAS8-03060.

REFERENCES

- Abdo, A. A., Ackermann, M., Ajello, M., et al. 2009, *Science*, **325**, 840
- Braje, T. M., Romani, R. W., Roberts, M. S. E., & Kawai, N. 2002, *ApJ*, **565**, L91
- Hartman, R. C., Bertsch, D. L., Bloom, S. D., et al. 1999, *ApJS*, **123**, 79
- Johnston, S., Hobbs, G., Vigeland, S., et al. 2005, *MNRAS*, **364**, 1397
- Ng, C.-Y., & Romani, R. W. 2007, *ApJ*, **660**, 1357
- Oka, T., Kawai, N., Naito, T., et al. 1999, *ApJ*, **526**, 764
- Ray, P. S., Kerr, M., Parent, D., et al. 2011, *ApJS*, **194**, 17
- Roberts, M. S. E., & Brogan, C. L. 2008, *ApJ*, **681**, 320
- Roberts, M. S. E., Romani, R. W., & Kawai, N. 2001, *ApJS*, **133**, 451
- Romani, R. W., & Watters, K. P. 2010, *ApJ*, **714**, 810
- van der Swaluw, E., Downes, T. P., & Keegan, R. 2004, *A&A*, **420**, 937